

## Imaging System Performance and Visibility as Affected by the Physical Environment

Grace Chang  
Sea Engineering, Inc.  
200 Washington St., Suite 101  
Santa Cruz, CA 95060

Phone: (831) 421-0871 Fax: (831) 421-0875 Email: [gchang@seaengineering.com](mailto:gchang@seaengineering.com)

Award Number: N00014-11-M-0144

### LONG-TERM GOALS

The long-term goals of “Radiance in a Dynamic Ocean (RaDyO): Radiance and Visibility as Affected by Inherent Optical Properties” (award number N0001409C0443) and “Imaging System Performance and Visibility as Affected by the Physical Environment” were to perform detailed investigations of inherent optical properties (IOPs) and the effects of IOP variability on underwater radiance and visibility and to investigate the relationships between physical forcing and optical properties, including the imaging performance parameters. These efforts were aimed at supporting the Radiance in a Dynamic Ocean (RaDyO) program, which was devoted to the topic of light propagation and imaging across the air-sea interface and within the surface boundary layer of natural water bodies.

### OBJECTIVES

The objectives of these RaDyO projects were to:

- (1) Investigate the differences between optical properties and optical variability measured off the R/P FLIP and off the R/V Kilo Moana (KM) during the RaDyO Santa Barbara Channel (SBC) experiment and the effects of optical variability on the modeling of the underwater radiance distribution and visibility.
- (2) Determine the relationships between physical processes and the optical properties that affect underwater visibility and the imaging performance parameters.
- (3) Investigate the effects of vertical variability (e.g., vertical layering) of optical properties on the image performance parameters, i.e. modulation transfer function (MTF) and point spread function (PSF).

### APPROACH

#### *Objective (1)*

Concurrent profiles of optical properties collected off the FLIP and the KM during the SBC experiment were analyzed for optical variability. The datasets from the two platforms were merged with depth and density and compared. Percent differences between KM and FLIP measurements were computed according to:

$$\% \text{ Difference} = [ (X_{\text{KM}} - X_{\text{FLIP}}) / (X_{\text{KM}} + X_{\text{FLIP}}) / 2 ] * 100, \quad (1)$$

## Report Documentation Page

*Form Approved  
OMB No. 0704-0188*

Public reporting burden for the collection of information is estimated to average 1 hour per response, including the time for reviewing instructions, searching existing data sources, gathering and maintaining the data needed, and completing and reviewing the collection of information. Send comments regarding this burden estimate or any other aspect of this collection of information, including suggestions for reducing this burden, to Washington Headquarters Services, Directorate for Information Operations and Reports, 1215 Jefferson Davis Highway, Suite 1204, Arlington VA 22202-4302. Respondents should be aware that notwithstanding any other provision of law, no person shall be subject to a penalty for failing to comply with a collection of information if it does not display a currently valid OMB control number.

1. REPORT DATE <b>30 SEP 2013</b>	2. REPORT TYPE	3. DATES COVERED <b>00-00-2013 to 00-00-2013</b>		
4. TITLE AND SUBTITLE <b>Imaging System Performance and Visibility as Affected by the Physical Environment</b>			5a. CONTRACT NUMBER	
			5b. GRANT NUMBER	
			5c. PROGRAM ELEMENT NUMBER	
6. AUTHOR(S)			5d. PROJECT NUMBER	
			5e. TASK NUMBER	
			5f. WORK UNIT NUMBER	
7. PERFORMING ORGANIZATION NAME(S) AND ADDRESS(ES) <b>Sea Engineering, Inc,200 Washington St., Suite 101,Santa Cruz,CA,95060</b>			8. PERFORMING ORGANIZATION REPORT NUMBER	
			9. SPONSORING/MONITORING AGENCY NAME(S) AND ADDRESS(ES)	
11. SPONSOR/MONITOR'S REPORT NUMBER(S)				
12. DISTRIBUTION/AVAILABILITY STATEMENT <b>Approved for public release; distribution unlimited</b>				
13. SUPPLEMENTARY NOTES				
14. ABSTRACT				
15. SUBJECT TERMS				
16. SECURITY CLASSIFICATION OF:			17. LIMITATION OF ABSTRACT <b>Same as Report (SAR)</b>	18. NUMBER OF PAGES <b>14</b>
a. REPORT <b>unclassified</b>	b. ABSTRACT <b>unclassified</b>	c. THIS PAGE <b>unclassified</b>		
19a. NAME OF RESPONSIBLE PERSON				

where X is temperature, salinity,  $a_g(\lambda)$ ,  $a_{pg}(\lambda)$ ,  $c_{pg}(\lambda)$ ,  $b_{bp}(\lambda)$ ,  $\gamma$ , or  $n_p$  as a function of depth and as a function of  $\sigma_t$  ( $a_{pg}(\lambda)$  and  $c_{pg}(\lambda)$  are the particulate plus dissolved absorption and attenuation coefficients, respectively).

To first-order, the relationship presented by Davies-Colley (1988) and further examined by Zaneveld and Pegau (2003) was used to estimate the horizontal visibility of a black target,  $y$ :

$$y = 4.8 / \alpha, \quad (2)$$

where  $\alpha$  is the photopic beam attenuation coefficient, which is a function of the spectral background radiance and the distance between the target and the observer. It was approximated by (Zaneveld and Pegau, 2003):

$$\alpha = c_{pg}(532) * 0.9 + 0.081. \quad (3)$$

In this regard, only one of the IOPs, the beam attenuation coefficient at 532 nm, was necessary for predictions of horizontal visibility of a black target. Equations (2) and (3) were applied to IOP data collected during low wind, stratified conditions ( $< 5 \text{ m s}^{-1}$ ) and high wind, mixed conditions ( $\geq 5 \text{ m s}^{-1}$ ) and used to examine the differences in predicted visibility.

### *Objective (2)*

The MTF, which is the magnitude of the Fourier transform of the PSF, was computed for two different water bodies using measurements of optical properties and analytical formulations described by Wells (1973) and Hou et al. (2007). The MTF of an aquatic medium,  $H(\psi, z)$ , can be represented by:

$$H(\psi, z) = e^{-D(\psi)Z}, \quad (4)$$

where  $Z$  is the range,  $D(\psi)$  is the decay transfer function (DTF), and  $\psi$  is spatial frequency. By application of small-angle scattering approximations (Wells, 1973) the collimated DTF can be approximated as:

$$D^c(\psi) = c - S(\psi), \quad (5)$$

where  $c$  is the beam attenuation coefficient and  $S(\psi)$  is the light scattered back into the acceptance cone:

$$S(\psi) = 2\pi \int_0^{\theta_{\max}} J_0(2\pi\theta\psi) \beta(\theta) \theta d\theta, \quad (6)$$

where  $\beta(\theta)$  is the volume scattering function (VSF),  $\theta$  is the scattering angle, and  $J_0$  is the zero-order Bessel function. The desired focused DTF can then be obtained by transformation in terms of spatial frequency ( $2\pi\theta\psi$ ) (see Wells, 1973 for more details):

$$D(\psi) = \int_0^1 D^c(\psi t) dt. \quad (7)$$

In situations where the VSF may not be quantified, the following assumptions about the VSF have been made (e.g., Wells, 1973):

$$\beta(\theta) = (b \theta_o) / [2\pi (\theta_o^2 + \theta^2)^{3/2}], \quad (8a)$$

where  $\theta_o$  is mean square angle and  $b$  is the scattering coefficient:

$$b = 2\pi \int_0^{\pi} \beta(\theta) \sin \theta d\theta; \quad (8b)$$

therefore a closed-form solution for the MTF is possible without direct measurements of the VSF:

$$D(\psi) = c - [b (1 - e^{-2\pi \theta_o \psi})] / (2\pi \theta_o \psi). \quad (9)$$

The optical data necessary for MTF computations were collected from two field sites as part of the ONR sponsored RaDyO program: (1) Scripps Institution of Oceanography (SIO) Pier, a shallow-water, eutrophic environment and (2) the Santa Barbara Channel (SBC), a deeper, mesotrophic environment (Chang et al., 2010). Profiler measurements were used to compute optical products: backscattering

ratio,  $\tilde{b}_{bp}(\lambda) = b_{bp}(\lambda)/b_p(\lambda)$ ; the slope of the  $c_p(\lambda)$  spectrum,  $\gamma$ , an indicator of particle size distribution (Boss et al., 2001); the real part of the index of refraction of particles,  $n_p$ , from  $\gamma$  and  $\tilde{b}_{bp}(\lambda)$  (Twardowski et al., 2001), useful for obtaining information about the relative density of particles; the single-scattering albedo,  $\omega_o = b / c$ ; and chlorophyll concentration (Chl) from chlorophyll fluorescence and spectral absorption using the methods of Sullivan et al. (2005). The MASCOT data (M. Twardowski; WET Labs, Inc.) were used to compute a “bubble index” (BI), where  $BI = \beta(70^\circ) / \beta(120^\circ)$ . This BI is based on theoretically computed VSFs of relatively large bubbles ( $> 10 \mu\text{m}$ ), which show pronounced enhancement of the VSF between  $60^\circ$  and  $80^\circ$  (Czerski et al., 2011; Twardowski et al., 2012). Hence, increases in the BI can be indicative of a relative increase in the concentration of larger bubbles.

Relationships between physical, hydrographic, and optical properties and the imaging performance parameter, MTF, were determined for the SBC experiment by use of wavelet analysis. Continuous wavelet transforms (CWTs), cross wavelet transforms (XWTs), and wavelet coherence (WTC) are useful tools for analyzing localized, intermittent oscillations in data series, as well as the relationship and linkages between two data series and the strength of the relationship(s) (see Grinsted et al., 2004). Fourier expansion (e.g., fast Fourier transform; FFT) has traditionally been the technique employed for determining the frequencies present in a signal. However, FFTs have only frequency resolution and no time resolution. In other words, although FFTs can reveal all frequencies present in a signal, they cannot determine when these frequencies are present in time. Similar to this, coherence analysis can be used to find common periodicities between two different time series; however, determined commonality is not localized in time or space. Wavelet analysis can be utilized to expand data series into time-frequency space and thus identify localized intermittent periodicities at multiple frequency and temporal resolutions.

### *Objective (3)*

The MTF of seawater was computed using profiled measurements of IOPs conducted between the near-surface and 30 m water depth in SBC and Equations (4) through (9) (see Chang et al., 2010 and Chang and Twardowski, 2011). The effects of stratification and scattering layers on the MTF were examined for two different scenarios (Figure 1):

- A. A virtual imager located at the surface and virtual targets at ranges between 10 cm and 30 m below the source.
- B. Virtual imagers located between the surface and 30 m and the targets located 10 cm below the imagers.

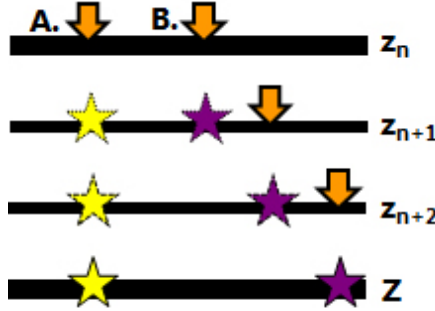


**Figure 1. Schematic diagram of two scenarios: A (left). Virtual imager (arrow) and virtual targets (stars) separated by scattering layers,  $z_n$ , over a total distance,  $Z$ , and B (right). Virtual imagers located a distance,  $z_n$ , above virtual targets.**

For scenario A (Figure 1, left), the collimated decay transfer function (DTF),  $D^c(\Psi)$ , and MTF,  $H(\Psi)$ , at range,  $Z$ , and spatial frequency,  $\psi$ , were computed following:

$$D^c(\Psi)_s = c - \int_{z_1/Z}^{z_2/Z} S(\Psi, z) dz$$

where the  $s$  denotes the scattering layer,  $c$  is the beam attenuation coefficient of layer  $s$ ,  $S$  is the light scattered back to the acceptance cone of layer  $s$ , and an integral taken between the imager and distances  $z_1$ , and  $z_2$  over a total range of  $Z$  to the target.

$$S(\Psi) = 2\pi \int_0^{\theta_{\max}} J_0(2\pi\theta\Psi) \beta(\theta) \theta d\theta$$

where  $\beta(\theta)$  is the volume scattering function (VSF),  $\theta$  is the scattering angle, and  $J_0$  is the zero-order Bessel function. The near-forward VSF was measured using a LISST-100X and measurements of the beam attenuation coefficient were provided by an ac-s. The focused DTF was obtained by transformation in terms of spatial frequency ( $2\pi\theta\Psi$ ) prior to computation of the MTF (Wells, 1973):

$$D(\Psi) = \int_0^1 D^c(\Psi t) dt$$

$$H(\Psi, z)_s = e^{-[D_1(\Psi)z_1 + D_2(\Psi)z_2 + \dots]}$$

Vertical profiles of the MTF at a spatial frequency equal to  $1.0 \text{ rad}^{-1}$  were constructed using the equation for  $H(\Psi, z)_s$  above by summing the DTFs between the surface and each  $z_n = 10 \text{ cm}$  layer to a maximum range of  $Z = 30 \text{ m}$ .

The DTF and MTF for scenario B (Figure 1, right) were calculated following:

$$D(\Psi) = c - S(\Psi)$$

$$H(\Psi, z) = e^{-D(\Psi)z}$$

where  $z$  is the range of each layer (e.g.,  $z_{n+2}$  to  $Z$ ), with similar transformation to the focused DTF. In case B, the vertical profile of the MTF for  $\Psi$  equal to  $1.0 \text{ rad}^{-1}$  was constructed with multiple virtual imagers and targets, all separated by the same distance (10 cm) (Figure 1).

Scattering layer effects on the MTF for the two different scenarios were quantified by:

- Applying a power-law fit,  $\gamma$ , to the MTF at a given spatial frequency as a function of depth.
- Determining the extinction depth,  $\kappa$ , of MTF, where the extinction depth was defined as the depth at which the MTF decreased to 0.01 cycles/rad.

## WORK COMPLETED

All work described above was completed. Results are summarized below.

## RESULTS

### Objective (1)

A diurnal wind pattern was observed during the two-week SBC experiment. Winds were generally calm (< 4 m/s) in the mornings, and increased to greater than 6 m/s, oftentimes reaching 10 m/s by 1600 PDT. Starting on 15 September, winds greater than about 5 m/s were sustained over the course of two days. The persistent winds resulted in increased upper water column mixing, as evidenced by the increase in 30 m temperature and salinity and the deepening of the mixed layer depth.

The majority of optical variability between the FLIP and the KM was due primarily to platform effects, specifically the break-down of stratification from mixing by the hull of R/P FLIP when winds were less than 5 m/s (Figure 2; Chang et al., 2010). Differing vertical patterns in hydrographic properties and dissimilar vertical distributions of water constituents (and therefore optical properties) observed between the KM and FLIP were the consequence of FLIP-induced mixing. The FLIP-effect was not a factor during higher wind speeds, as the upper water column was well-mixed at both platform locations.

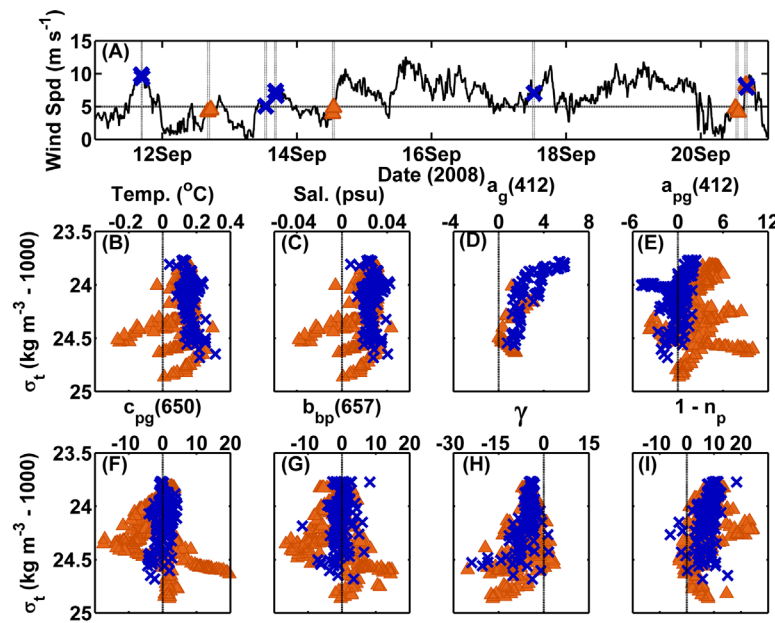


**Figure 2.** (A) Time series of wind speed. Crosses and triangles indicate periods of data collection. (B-I) Profiles of percent differences between properties measured from the KM versus from the FLIP as a function of  $\sigma_t$ . The units for  $a_g(412)$ ,  $a_{pg}(412)$ ,  $c_{pg}(650)$ , and  $b_{bp}(657)$  are  $m^{-1}$ . Crosses indicate periods of data collection with wind speeds  $\geq 5$  m/s and triangles represent wind speeds  $< 5$  m/s (except the last profile).

The observed variable vertical distributions in optical properties greatly affected modeled underwater radiance distribution and predictions of horizontal visibility (Figure 3). Hydrolight-modeled radiometric properties and AOPs differed by about 50% between the KM and FLIP sites during

stratified, low wind conditions, as compared to less than 10% during well-mixed periods. The attenuation-based model presented by Zaneveld and Pegau (2003) and a backward Monte-Carlo model were used to predict the horizontal visibility of a black target for high wind and low wind conditions. Results from both models were consistent. The results show that highly variable IOPs observed between the FLIP and KM during low winds can affect predictions of visibility by up to 57%. Differences were less than 15% between KM and FLIP predicted visibility range during well-mixed periods.

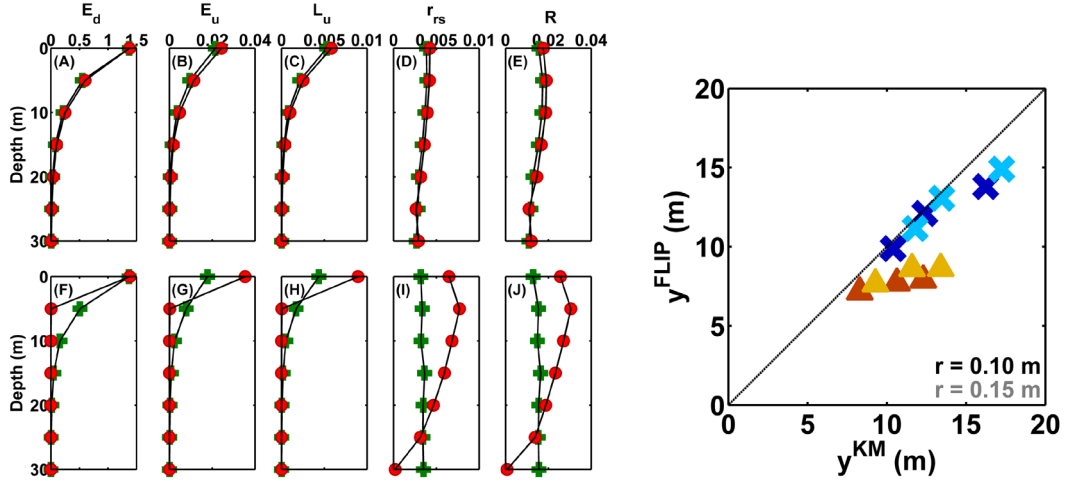


**Figure 3. Left:** Vertical profiles of radiometric and AOPs modeled using Hydrolight during (A-E) high wind conditions and (F-J) low wind conditions. Pluses represent KM data and y circles denote FLIP data. Units for  $E_d$  and  $E_u$  are  $W m^{-2} nm^{-1}$ , for  $L_u$  are  $W m^{-2} nm^{-1} sr^{-1}$ , and for  $r_{rs}$  is  $sr^{-1}$  ( $R$  is dimensionless). **Right:** Comparisons between computed horizontal visibility of a black target,  $y$ , using data collected from the KM versus from the FLIP. Crosses and triangles denote data collected during high wind and low wind conditions, respectively. Dark and light symbols signify results for targets with a diameter of 0.2 and 0.3 m (radius of 0.1 and 0.15 m), respectively.

### Objective (2)

Variability of near-surface MTF at both field sites was strongly influenced by physical forcing – meteorological processes in the SBC and rip currents at SIO Pier. The 2-week SBC field experiment can be partitioned into three distinct periods: (1) diurnal winds (11 – 15 September), (2) persistent strong winds and upper water column mixing (15 – 18 September), and (3) an advection event characterized by relatively high Chl and elevated optical quantities (19 – 21 September) (Figure 4). During diurnal winds and the sustained strong wind event in the SBC, higher wind speeds were associated with particle characteristics indicative of larger, non-pigmented particles with higher relative indices of refraction and decreases in the MTF. The presence of larger particles with higher index of refraction observed during the high winds of the SBC RaDyO experiment could have been the result of wind-induced mixing of the upper water column waters and surface bubble injection or an increase in non-chlorophyll containing particles (perhaps mineralogenic particles or senescent diatoms) or a combination of both of these factors. Anderson et al. (2008) and references therein have reported on phytoplankton succession in the SBC, with diatom dominance during upwelling periods (spring and summer), followed by continued surface depletion of nutrients and stratification, and likely diatom

sinking in the autumn. It is possible that these senescent diatoms were retained in near surface waters during strong mixing associated with high winds.

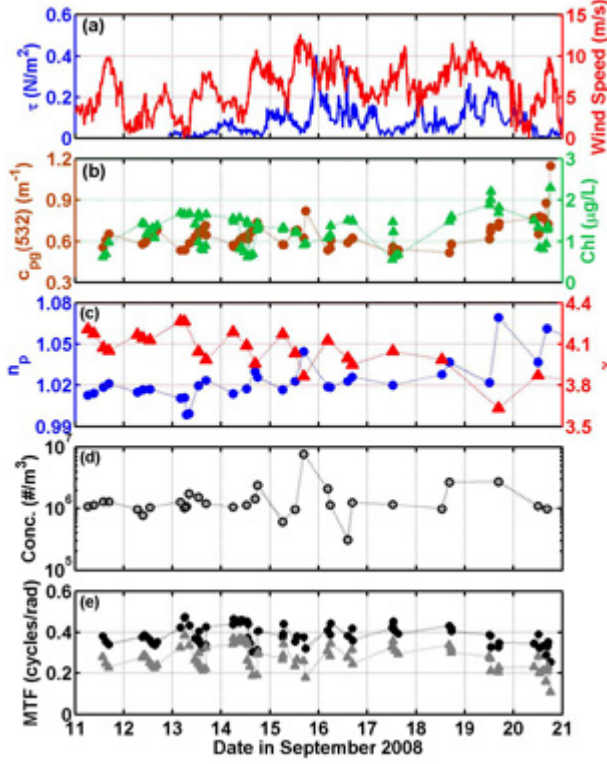


**Figure 4.** Time series of (a) wind stress (blue) and wind speed (red), (b)  $c_{pg}(532)$  (brown dots) and Chl (green triangles) at 2 m, (c) near-surface  $n_p$  (blue dots) and  $\gamma$  (red triangles), near-surface (d) volumetric bubble concentration derived from BI, and (e) MTF for  $\Psi = 3 \text{ rad}^{-1}$  (black dots) and  $\Psi = 50 \text{ rad}^{-1}$  (gray triangles) calculated from 2 m optical data collected in the SBC.

Surface bubble injection is often associated with strong sustained winds, which in itself would result in substantive changes in particle composition characteristics in surface waters (Zhang et al., 2011). Information about bubble concentration was obtained from the BI, which was derived from the ratio of MASCOT-measured VSFs at  $70^\circ$  and  $120^\circ$ . The BI can be used as a proxy for the concentration of the large bubble subpopulation, following Twardowski et al. (2012). The derived concentration of relatively large bubbles ( $> 10 \mu\text{m}$  in diameter) increased by nearly an order of magnitude on 15 September 2008 and by a factor of three on 18 September, coinciding with periods of sustained elevated wind speeds (Figure 4d). The increase in the concentration of the large bubble subpopulation was accompanied by a decrease in the slope of the particulate attenuation spectra, indicative of an increase in particle size (Figure 4c).

Although not statistically significant in 2-m time series data, the observed advection/bloom event starting on 19 September 2008 resulted in significant coherence between the MTF and the IOPs and IOP products indicative of particle concentration and composition at about 20-m water depth. This event was marked by a decrease in the MTF, increases in the magnitude of all IOPs, Chl, and  $n_p$  and a decrease in  $\gamma$ , indicative of an increase in the concentration of larger biogenic particles with relatively higher refractive index (Figure 4). The concentration of the large bubble subpopulation during this

time period was relatively low, suggesting lesser effects due to surface bubble injection and more to a phytoplankton bloom that was associated with a shift in the SBC circulation (Figure 4).

Highly reflective mineralogenic particles with relatively high bulk particle index of refraction were associated with SIO Pier rip currents, which resulted in a large increase in the MTF. These particles, although not explicitly sampled or analyzed, appeared like mica flakes, which although rare in beach sand, have been observed along beaches in San Diego, CA. This increase in the MTF was likely due to enhanced reflectivity coupled with relatively high visibility; beam attenuation was not greatly elevated during the rip current event and Chl was at a minimum (Figure 5).

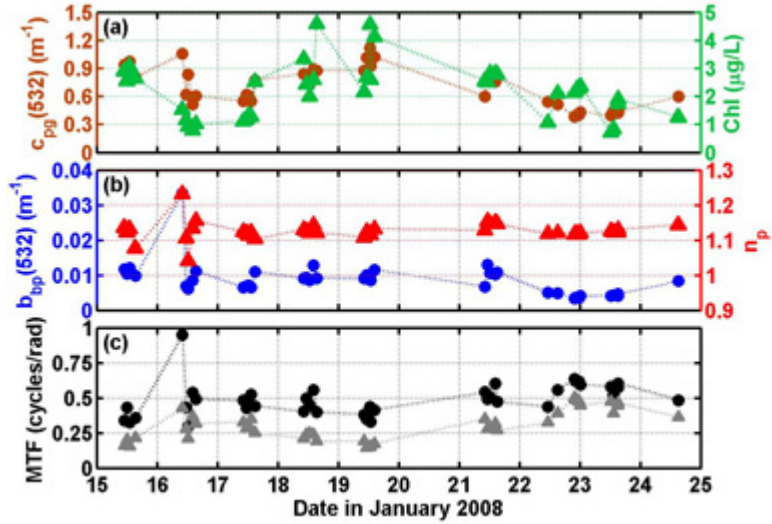


**Figure 5. SIO Pier time series of 2-m (a)  $c_{pg}(532)$  (brown dots) and Chl (green triangles) and (b)  $b_{bp}(532)$  (blue dots) and  $n_p$  (red triangles); and (c) MTF ( $\Psi = 3 \text{ rad}^{-1}$  in black dots and  $\Psi = 50 \text{ rad}^{-1}$  in gray squares).**

These observations are particularly interesting as one would expect the imaging performance parameter to be influenced primarily by particle concentration as revealed by the magnitude of IOPs; however it was found that particle size and type (relative density information gained from the real index of refraction of particles) were important sources of variability in the MTF.

The results show that the effects of particle composition on the shape of the VSF in the near-forward direction are important to imaging performance, which is a unique observation facilitated by advancements in *in situ* optical instrumentation. By performing a sensitivity analysis using the  $\beta$ -approximation formulation for the MTF, the relative importance of particle effects on the MTF was determined (Figure 6). Results suggest that at  $\theta_o$  between 0.07 and 0.11 rad, particle concentration and composition affected MTF variability similarly. At  $\theta_o$  greater than 0.11 rad, MTF variability was stronger with variable IOPs, i.e. particle concentration effects dominated. Strikingly, when  $\theta_o$  is between 0.03 and 0.07 rad (i.e. particle size distributions trending toward larger sizes), the MTF is much higher for frequencies less than  $30 \text{ rad}^{-1}$  (Figure 6). Here, particle composition effects dominated MTF variability, in a relative sense. For the specific ranges of variability in optical properties observed during the study, these modeling results are consistent with the strong coherence observed between particle composition parameters and imaging performance.

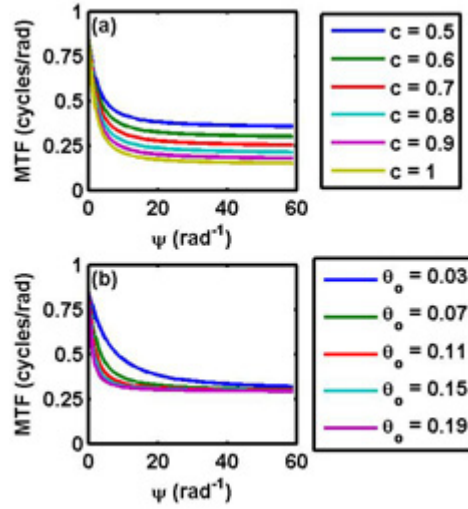


**Figure 6. Particle concentration versus composition effects on MTF variability.** (a) MTF computed by varying the beam attenuation coefficient,  $c$  (as indicated), while keeping the mean square angle,  $\theta_0$ , constant at  $0.07 \text{ rad}$ . (b) MTF computed by varying  $\theta_0$  (as indicated) while keeping  $c$  constant at  $0.6 \text{ m}^{-1}$ . The range was set at  $2 \text{ m}$  and  $\omega_0$  was  $0.9$  in both situations.

The small-angle approximation (Eq. 8; e.g., Wells, 1973) assumes strong forward scattering, which was not the case during the SIO Pier rip currents. To explore this further, MTFs computed from the DTF using measured  $\beta$  (Eq. 7) were evaluated versus those calculated using approximated  $\beta$  (Eq. 9;  $\theta_0 = 0.07 \text{ rad}$ ) for the SIO Pier data set (Figure 7). The  $\beta$ -approximation method produced very similar MTFs to those computed using measured  $\beta$ , particularly at high spatial frequencies ( $> 10 \text{ rad}^{-1}$ ). MTFs at spatial frequencies less than  $10 \text{ rad}^{-1}$  were not comparable during periods when the backscattering coefficient exceeded  $0.012 \text{ m}^{-1}$ . Results from the two methods deviated greatly from each other at all spatial frequencies during the rip current event (Figure 7). Here, it is shown that in highly backscattering environments such as those with substantial mineralogenic particles, the shape of the VSF cannot be assumed when computing imaging performance parameters such as the MTF.

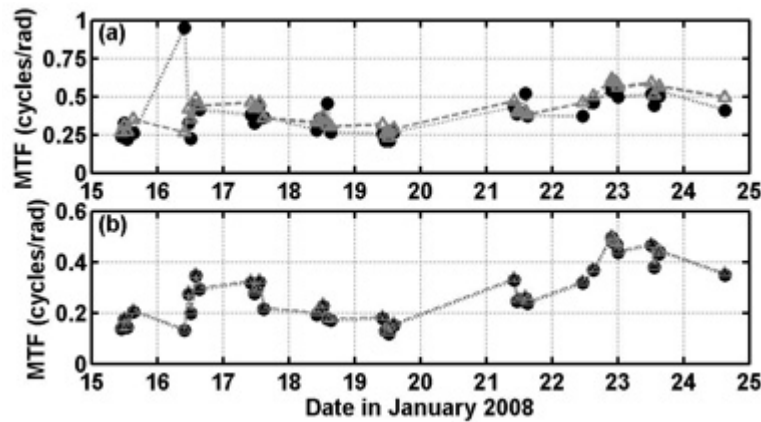


**Figure 7. SIO Pier time series of MTF at  $\Psi = (a) 3 \text{ rad}^{-1}$  and (b)  $50 \text{ rad}^{-1}$ , with MTFs computed using the  $\beta$ -approximation (e.g., Wells, 1973) shown with gray triangles.**

### Objective (3)

The upper water column MTF at small spatial frequencies in the presence of scattering layers and stratification can be orders of magnitude less than the MTF in mixed conditions, as illustrated in Figure 8. The distance between the imager and target contributed greatly to the magnitude of the MTF when imager and target were separated by a scattering layer.

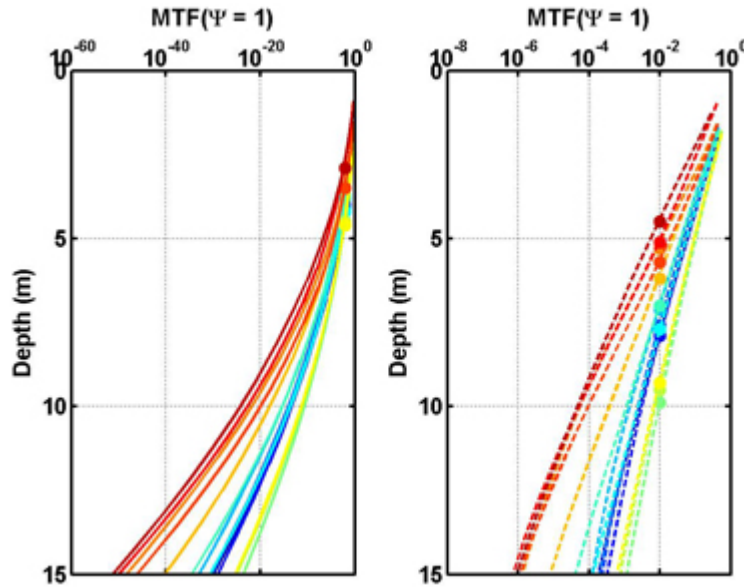


**Figure 8.** Vertical profiles of the  $MTF(\Psi = 1 \text{ rad}^{-1})$  shown to a range of  $Z = 15 \text{ m}$  for A: Scenario A and B: Scenario B. The solid dots indicate the extinction depth,  $\kappa$ . Profile color-coding denotes specific periods of the SBC RaDyO experiment: blues = strong stratification, yellow-green = upper water column mixing, and reds = strong scattering layers from localized upwelling (see Chang et al., 2010 and Chang and Twardowski, 2011 for more details).

The extinction depth determined for the  $MTF(\psi = 1 \text{ rad}^{-1})$  with an imager at the surface (scenario A) did not vary greatly from about 4.5 m for all 15 profiles; the minimum value of  $\kappa$  was 2.9 m in the presence of strong scattering layers and maximum  $\kappa$  was 4.8 m during mixed conditions (Figure 9). When virtual imagers and targets were placed 10 cm apart throughout the water column,  $\kappa$  varied between 4.5 m (strong scattering layers) and 9.8 m (mixed conditions).

The differences in  $\gamma$  between scenarios A and B were larger during stratified conditions (average difference of 1.5) as compared to during upper water column mixed conditions (average difference of 1.25). The smallest difference in  $\gamma$  between scenarios A and B (0.985) occurred during periods with strong scattering layers (Figure 9).

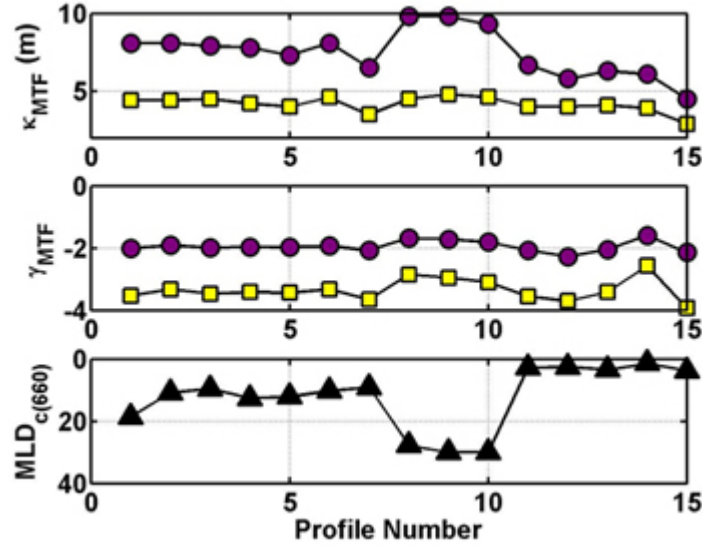


**Figure 9.** Upper:  $MTF(\Psi = 1 \text{ rad}^{-1})$  extinction depth, Middle: Slope of the power-law fit to the vertical profile of  $MTF(\Psi = 1 \text{ rad}^{-1})$ , and Lower: The mixed layer depth computed as the depth at which the  $c_{pg}(660)$  change from near-surface  $c_{pg}(660)$  is greater than  $0.05 \text{ m}^{-1}$ . Yellow = scenario A and Purple = scenario B. The profile numbers can be characterized by: 1-7 = strong stratification, 8-10 = mixed, and 11-15 = strong scattering layers.

These results imply that in the presence of near-surface optical scattering layers, an underwater image taken from just below the surface to a depth of a mere 0.5 m can be significantly blurrier than if the imager was located tens of cm below the surface. Additionally, analysis or reconstruction of an image taken by a near-surface detector of a target located at just a couple of meters below the surface may not be possible in the presence of strong scattering layers, even if the water appears relatively clear from the surface.

## IMPACT/APPLICATIONS

### *Objective (1)*

The results have the potential to greatly impact the modeling of underwater radiance distribution for the RaDyO project. The hull of FLIP itself has the capability to mix the upper water column and affect SBL processes. Physical measurements conducted by RaDyO PIs off the FLIP could have been compromised. Additionally, IOPs were not collected off the FLIP during the Hawaii experiment; hence the model(s) would have been constructed and/or validated with physical, radiometric, and apparent optical property (AOP) measurements collected off the FLIP and IOP measurements collected off the KM, which was several km away.

### *Objective (2)*

Optically-derived particle characteristics such as bulk particle index of refraction and particle size distribution were shown to be significantly related to the variability of the MTF. This, in addition to the great temporal variability in environmental conditions observed at two different field sites stresses the importance of obtaining or predicting optical properties and derived particle composition characteristics (describing relative particle size and type) at temporal and spatial scales necessary to

quantify rapid changes in image processing parameters. Importantly, estimates of water clarity or turbidity are not the only factors influencing the variability of the image performance parameters, particularly at steep near-forward scattering angles, where variability in the MTF was found to be dominated by particle composition effects. Additionally, the standard approximation for the VSF cannot be used to compute imaging performance in environments with highly backscattering/reflective particles.

#### *Objective (3)*

Knowledge of the MTF is important for the interpretation of images from underwater electro-optical imaging systems. MTF-based image analysis and reconstruction is influenced by optical inhomogeneity (i.e. scattering layers) as well as by the vertical placement of the target versus that of the detector, or imager (Wells, 1973; Frew and Voss, 1997). Take, for example, the remark made by Wells (1973), “You can lay a sheet of vellum on a printed page and read through it quite well, but the same vellum lifted a centimeter off the page completely obscures vision.” This statement is now outdated as vellum is no longer a common source for paper. Here is another way to consider the problem: one should not feel embarrassed while showering several feet away from a textured shower door; however body parts could be fully revealed should they make contact with the door (Figure 10).

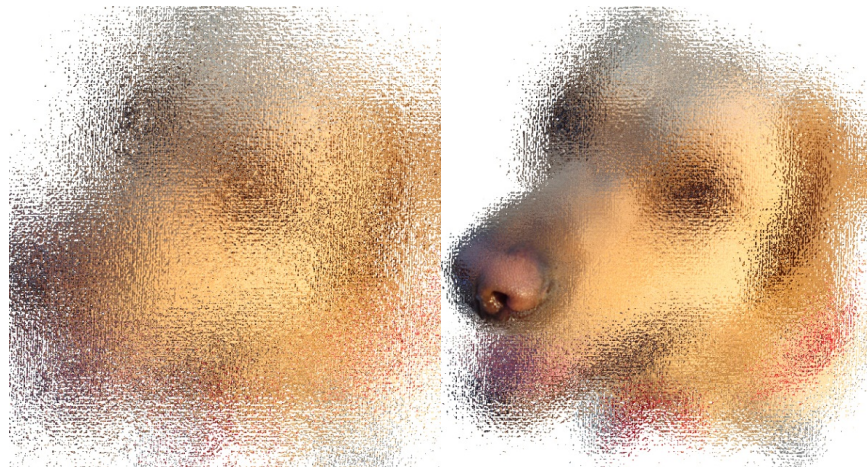


**Figure 10.** These photographs of Peso the dog were manipulated in Photoshop to simulate Peso well behind a textured glass shower door (Left) and Peso's nose pressed against the glass (Right).

This same effect applies in stratified ocean environments where a target and imager are separated by optically distinct layers. These layers could have important implications on imaging performance and analysis. The ability to determine optimal placement of passive imagers relative to target locations would constitute dramatic improvements to image clarity and restoration efforts. Additionally, image reconstruction would be facilitated with knowledge of the effects of scattering layers on image distortion and imaging performance parameters.

## **RELATED PROJECTS**

At present, none.

## REFERENCES

Anderson, C. R., D. A. Siegel, M. A. Brzezinski, and N. Guillocheau (2008), Controls on temporal patterns in phytoplankton community structure in the Santa Barbara Channel, California, *J. Geophys. Res.*, 113, C04038, doi:10.1029/2007JC004321.

Boss E., M. S. Twardowski, and S. Herring (2001) Shape of the particulate beam attenuation spectrum and its inversion to obtain the shape of the particle size distribution, *Appl. Opt.*, 40, 4885-4893.

Chang, G. and M. S. Twardowski (2011) Effects of physical forcing and particle characteristics on underwater imaging performance, *J. Geophys. Res.*, 116, C00H03, doi:10.1029/2011JC007098.

Chang, G., M. S. Twardowski, Y. You, M. Moline, P.-W. Zhai, S. Freeman, M. Slivkoff, F. Nencioli, and G. W. Kattawar (2010) Platform effects on optical variability and prediction of underwater visibility, *Appl. Opt.*, 49(15), 2784-2796.

Czerski, H., M. Twardowski, X. Zhang, and S. Vagle (2011) Resolving size distributions of bubbles with radii less than 30  $\mu\text{m}$  with optical and acoustical methods, *J. Geophys. Res.*, 116, C00H11, doi:10.1029/2011JC007177.

Davies-Colley, R. J. (1988) Measuring water clarity with a black disk, *Limnol. Oceanogr.*, 33, 616-623.

Frew, B. and K. Voss (1997) Measurement of the point-spread function in a layered system, *Appl. Opt.*, 36, 3335-3337.

Grinsted, A., J. C Moore, and S. Jevrejeva (2004) Application of the cross wavelet transform and wavelet coherence to geophysical time series, *Nonlin. Proc. in Geophys.*, 11, 561-566.

Hou, W., Z. Lee, and A. D. Weidemann (2007) Why does the Secchi disk disappear? An Imaging perspective, *Opt. Expr.*, 15, 2791-2802.

Sullivan, J., M. S. Twardowski, P. L. Donaghay, and S. A. Freeman (2005) Using Scattering Characteristics to Discriminate Particle Types in US Coastal Waters, *Appl. Opt.*, 44, 1667-1680.

Twardowski, M. S., E. Boss, J. B. Macdonald, W. S. Pegau, A. H. Barnard, and J. R. V. Zaneveld (2001) A model for estimating bulk refractive index from the optical backscattering ratio and the implications for understanding particle composition in case I and case II waters, *J. Geophys. Res.*, 106, 14,129-14,142.

Twardowski, M., X. Zhang, S. Vagle, J. Sullivan, S. Freeman, H. Czerski, Y. You, L. Bi, and G. Kattawar (2012) The optical volume scattering function in a surf zone inverted to derive sediment and bubble particle subpopulations, *J. Geophys. Res.*, doi:10.1029/2011JC007347.

Wells, W. H. (1973) Theory of small angle scattering, in AGARD Lec. Series No. 61, pp. 3.3.1 – 3.3.19, NATO, Neuilly-sur-Seine, France.

Zaneveld, J. R. V. and W. S. Pegau (2003) Robust underwater visibility parameter, *Opt. Expr.*, 11, 2997-3009.

Zhang, X., M. Twardowski, and M. Lewis (2011), Retrieving composition and sizes of oceanic particle subpopulations from the volume scattering function, *Appl. Opt.*, 50, 1240-1259.

## PUBLICATIONS

Chang, G., M. S. Twardowski, Y. You, M. Moline, P.-W. Zhai, S. Freeman, M. Slivkoff, F. Nencioli, and G. W. Kattawar (2010) Platform effects on optical variability and prediction of underwater visibility, *Appl. Opt.*, 49(15), 2784-2796. [Published, Refereed]

Chang, G. and M. S. Twardowski (2011) Effects of physical forcing and particle characteristics on underwater imaging performance, *J. Geophys. Res.*, 116, C00H03, doi:10.1029/2011JC007098. [Published, Refereed]

Chang, G. (2012) Scattering layer effects on the modulation transfer function, *Proceedings of the Ocean Optics Conference (extended abstract)*, Glasgow, Scotland, October 2012.